Simple Model of Microsegregation during Solidification of Steels

YOUNG-MOK WON and BRIAN G. THOMAS

A simple analytical model of microsegregation for the solidification of multicomponent steel alloys is presented. This model is based on the Clyne–Kurz model and is extended to take into account the effects of multiple components, a columnar dendrite microstructure, coarsening, and the δ/γ transformation. A new empirical equation to predict secondary dendrite arm spacing as a function of cooling rate and carbon content is presented, based on experimental data measured by several different researchers. The simple microsegregation model is applied to predict phase fractions during solidification, microsegregation of solute elements, and the solidus temperature. The predictions agree well with a range of measured data and the results of a complete finite-difference model. The solidus temperature decreases with either increasing cooling rate or increasing secondary dendrite arm spacing. However, the secondary dendrite arm spacing during solidification decreases with increasing cooling rate. These two opposite effects partly cancel each other, so the solidus temperature does not change much during solidification of a real casting.

I. INTRODUCTION

SOLIDIFICATION phenomena play a major role in such diverse operations as casting, crystal growth, and welding. Solidification proceeds at various rates, which are sometimes far from equilibrium. Thus, the microstructure obtained is generally not homogeneous and gives rise to variations in composition with position at both small and large scales, which is known as segregation.

Solute segregation is important because it leads to nonequilibrium phases, cracks, and other problems, which lower the mechanical properties of the final product. Over the last three decades, attention has focused on segregation of aluminum and steel alloys, owing to their great commercial importance and susceptibility to this solidification problem. Segregation affects all processes, including foundry, ingot, and continuous casting.

Segregation is classified, according to its scale, as macrosegregation or microsegregation. Macrosegregation occurs on the scale of the grains or the entire casting and can be observed with the naked eye. It arises from large-scale fluid flow, caused by forced, natural, and solutal convection. It requires the transport of solute-rich or -poor liquid and solid phases during solidification over distances much larger than the dendrite arm spacing. One unavoidable cause is the interdendritic flow of liquid due to solidification shrinkage and changes in the liquid density. These density changes can be caused by temperature changes or by changes in the liquid composition.[1,2,3] Macrosegregation is also affected by nozzles, which direct the liquid; electromagnetic forces, which enhance mixing;[4,5,6] and by thermal or mechanical bulging or deformation of the casting during solidification.[7] Microsegregation refers to a composition variation within the columnar or equiaxed dendritic solidification structure, which has a length scale on the order of only a few micrometers. Clearly, macrosegregation prediction is very complex. Among many other things, it depends on an accurate prediction of microsegregation.

Microsegregation is caused by the redistribution of solute during solidification, as solute is generally rejected into the liquid.[8] Its fundamental cause is the difference between the thermodynamic equilibrium solubility of alloy elements in the different phases that coexist in the mushy region during solidification. This is combined with the inability of solid-state diffusion to fully return the composition to its equilibrium constant level after solidification is complete, owing to the short times and small diffusion coefficients involved. Quantitative prediction of these phenomena is complicated by several difficulties.

(1) Quantifying the equilibrium solubility of each phase as a function of temperature. This is traditionally done using partition coefficients, which are reasonable for low concentrations, but which require the full multicomponent phase diagram for complex systems or higher alloy contents.[9]
(2) Solving for diffusion transport within the solid phases, which requires knowledge of (a) the diffusion coefficients for each element, (b) the length scale, which depends on the solidifying microstructure and varies from the secondary to the primary dendrite arm spacing to the grain size, and (c) the cooling conditions, which depend on macroscopic heat conduction in the casting.
(3) Linking of the microsegregation phenomena with the fluid flow and associated macrosegregation. This is complicated, because flow occurs on at least three size scales, including flow within the interdendritic spaces, flow between grains, and flow in the bulk liquid.[10]
(4) Accounting for phase transformations such as the peritectic transformation in steel, eutectic formation in aluminum alloys, and precipitate formation.

The purpose of the present work is to develop, validate, and apply a fast and simple microsegregation model for the

YOUNG-MOK WON, formerly a Postdoctoral Research Associate, Department of Mechanical and Industrial Engineering, University of Illinois at Urbana-Champaign, is Researcher, Pohang Iron & Steel Co., Ltd., Gyungbuk, 790-785 Korea. BRIAN G. THOMAS, Professor, is with the Department of Mechanical and Industrial Engineering, University of Illinois at Urbana-Champaign, Urbana, IL 61801.

Manuscript submitted October 10, 2000.

solidification of multicomponent steel alloys, which can be incorporated into other macroscopic models such as those coupled with fluid flow or thermal-stress analysis. The solubility levels are based on liquidus temperatures and partition coefficients taken from available measurements for multicomponent steel alloys, as are the diffusion coefficients. To obtain the microstructural-length scales, an empirical equation is developed to quantify the secondary dendrite arm spacing as a function of carbon content and cooling rate, based on experimental measurements of the final microstructures. This is because microstructure prediction is a very difficult task which requires computationally intensive modeling methods such as of the phase field[11–16] and cellular automata.[9,17–20] The cooling history needed by the model is planned to be calculated by a separate model, so, in the present work, the cooling rate is simply input to match experiments or treated as a parameter. Linking of the model with flow is ignored. This simple model of microsegregation also takes into account the effects of coarsening and the δ/γ peritectic transformation.

To validate this simple microsegregation model, its predictions are compared with both relevant experimental measurements by previous researchers[17,21–30] and more-accurate finite-difference model calculations. Finally, the effects of cooling rate, secondary dendrite arm spacing, and steel composition on microsegregation are investigated in a parametric study.

II. PREVIOUS WORK

Many microsegregation models[8,10,17,18,31–38] with different assumptions and simplifications have been developed to predict solute redistribution and related phenomena. Numerous studies[8,31–34] on microsegregation models have been carried out for only binary alloys. Some studies[9,10,17–20,35–38] modeled microsegregation during solidification of steels by taking into account binary,[10,36] five,[17–20] or more[9,37,38] solute elements and the peritectic reaction.

The heart of most simple microsegregation models is the assumed relationship between alloy concentration and solid fraction. This relationship can be evaluated to generate the one-dimensional composition profile between adjacent dendrite arms. These different relationships are now discussed, in order of increasing complexity.

The Lever-rule model is an equilibrium solidification model, which assumes complete diffusion to equilibrium of all alloying elements in both the liquid and the solid phases, as follows:

$$C_{L,i} = \frac{C_{0,i}}{1 - (1 - k_i) f_S} \qquad [1]$$

where $C_{L,i}$ is the liquid concentration of a given solute element at the solid-liquid interface, $C_{0,i}$ is the initial liquid concentration, k_i is the equilibrium partition coefficient for that element, and f_S is the solid fraction. The Lever-rule model is usually inaccurate later during solidification, because diffusion in the solid phases is too slow, especially for larger solute atoms such as manganese.

The opposite limiting case to the Lever-rule model is the Scheil equation,[31] or the "nonequilibrium Lever rule." This model assumes no diffusion in the solid phase, complete diffusion in the liquid phase, and local equilibrium at the solid-liquid interface, as follows:

$$C_{L,i} = \frac{C_{0,i}}{(1 - f_S)^{1-k_i}} \qquad [2]$$

However, it is apparent that the Scheil equation does not adequately estimate the final solute concentration, because $C_{L,i}$ becomes infinite at $f_S = 1$. This model is only useful for very rapid solidification processes such as laser welding, where the cooling rates exceed 10^2 °C/s.[21]

In order to predict microsegregation during steel solidification, finite nonzero diffusion must be considered, at least in the solid phase. Many simple microsegregation models[32,33,34] have been proposed, which assume a fixed dendrite arm spacing, constant physical properties in the solid phase, thermodynamic equilibrium at the solid-liquid interface, and straight liquidus or/and solidus lines in the equilibrium phase diagram.[39–43] Brody and Flemings[32] have proposed a general form of this model that assumes complete diffusion in the liquid phase and incomplete back-diffusion in the solid phase, as follows:

$$C_{L,i} = C_{0,i}(1 + f_S(\beta_i k_i - 1))^{(1-k_i)/(\beta_i k_i - 1)} \qquad [3]$$

This general form introduces β_i as a back-diffusion parameter, which has been quantified by many researchers[32,33,34] in different ways. In the original Brody–Flemings model for a plate dendrite,[32]

$$\beta_i = 2\alpha_i \qquad [4]$$

where α_i is a Fourier number for solute element i.

$$\alpha_i = \frac{D_{s,i} t_f}{X^2} \qquad [5]$$

where $D_{S,i}$ is the diffusion coefficient of solute element i in the solid phase, t_f is the local solidification time, and X is the length scale of the microsegregation domain, usually taken to equal half of the secondary dendrite arm spacing (λ_{SDAS}):

$$X = \frac{\lambda_{\mathrm{SDAS}}}{2} \qquad [6]$$

Equations [3] through [6] are solved by assuming the known t_f history to predict $C_{L,i}$ and related microstructure parameters.[32] The Brody–Flemings model simplifies to the Scheil equation in Eq. [2] when $D_{S,i}$ approaches zero ($\beta_i = 0$). On the other hand, when diffusion in the solid phase is infinitely fast, this model should logically simplify to the other extreme: the Lever rule (Eq. [1]), which corresponds to $\beta_i = 1$. Clearly, the model with Eq. [4] is not physically reasonable when α_i is large and β_i exceeds 1, because it does not even conserve mass.

To satisfy this requirement, Ohnaka[33] presented a simple modification of β_i to replace Eq. [4]. It is based on comparison with approximate solutions of the diffusion equation for the plate dendrite, assuming a quadratic solute profile in the solid.

$$\beta_i = \frac{2\alpha_i}{1 + 2\alpha_i} \qquad [7]$$

A further modification was proposed[33] to account for coarsening and irregular-shaped microstructures, such as columnar dendrites, by doubling α as follows:

$$\beta_i = \frac{4\alpha_i}{1 + 4\alpha_i} \quad [8]$$

Ohnaka has compared concentration predictions using Eqs. [3] and [8] with other approximate solutions and showed that his model agreed better with the experimental data of Matsumiya *et al.*[17] than did predictions using Eq. [4]. However, Voller *et al.*[8] pointed out that the performance of this model under constant cooling conditions is significantly better than its performance under parabolic cooling conditions.

A different modification to ensure physical reasonability in the Brody–Flemings model ($0 < \beta_i < 1$) was proposed by Clyne and Kurz[34] by replacing Eq. [4] as follows:

$$\beta_i = 2\alpha_i\left(1 - \exp\left(-\frac{1}{\alpha_i}\right)\right) - \exp\left(-\frac{1}{2\alpha_i}\right) \quad [9]$$

However, Ohnaka[33] and Matsumiya *et al.*[17] criticized this model for its lack of a physical basis for intermediate values of β_i.

Although all of the previous equations for microsegregation are semiempirical, they are simple analytical models that can be very useful if applied with caution. Among them, the Clyne–Kurz model is likely the most popular. Kobayashi[35] obtained an exact analytical solution for microsegregation, assuming complete diffusion in the liquid phase, incomplete back-diffusion in the solid phase, a constant partition coefficient, a constant diffusion coefficient, and a parabolic solidification rate. Its predictive performance is better than the aforementioned analytical models,[35] particularly if the partition coefficient (k_i) and Fourier number (α_i) are small. But, this analytical solution has the disadvantage that all physical properties must be assumed to be constant and that the solidification time must be known accurately.

Matsumiya *et al.*[17] solved for interdendritic microsegregation using a one-dimensional finite-difference numerical method, taking into account the diffusion of solute in both the liquid and the solid phases and hexagonal morphologies to approximate the dendrites. Battle and Pehlke[36] developed a similar numerical model for plate dendrites and included coarsening of the dendrite arms. The approach of Matsumiya *et al.* has been developed further to consider the δ/γ transformation, which occurs during solidification of steels.[18] Wang and Beckermann[10] developed a unified solute-diffusion model for columnar and equiaxed dendritic alloy solidification, in which nucleation, growth kinetics, and dendrite morphology are taken into account. Miettinen[9,37,38] developed models and data for thermodynamic phase equilibria and diffusion for solidification of low-alloy steels and stainless steels. The predicted thermophysical properties from the melting temperature down to room temperature, including solidus temperatures, solute microsegregation, and ferrite contents, agree well with experimental measurements.[37] These models have been implemented into the commercial packages Thermo-Calc,[45] IDS,[9] and MAGMA.[46] Unfortunately, these models take longer to compute the solute-distribution profile or to couple with other models, so there is still a use for accurate, simpler models.

Voller and Beckermann[8] proposed that the effect of coarsening can be accounted for in one-dimensional microsegregation models by adding an additional term to the Fourier number, as follows:

$$\alpha_i^+ = \alpha_i + \alpha^C \quad [10]$$

This enhancement to the Fourier number accounts for the extra back-diffusion which would occur, considering the smaller arm spacing that actually exists during solidification before coarsening. Voller and Beckermann[8] showed that, across a wide range of cooling conditions, this model is able to match full coarsening model results by simply adopting a constant value of $\alpha^C = 0.1$. They explained that coarsening could be included in any microsegregation model by simply replacing the Fourier number with the parameter α_i^+.

III. SIMPLE MICROSEGREGATION MODEL

The present simple microsegregation model developed in this work solves Eqs. [3], [5], and [6] based on evaluating the Clyne–Kurz model for each solute element, modified, as suggested by Ohnaka,[33] to extend the model from plate to columnar dendrites and, as suggested by Voller and Beckermann[8] to account for coarsening as follows:

$$\beta_i = 2\alpha_i^+\left(1 - \exp\left(-\frac{1}{\alpha_i^+}\right)\right) - \exp\left(-\frac{1}{2\alpha_i^+}\right), \quad \text{where } \alpha_i^+ = 2(\alpha_i + \alpha^C) \text{ and } \alpha^C = 0.1 \quad [11]$$

This simple semiempirical analytical model assumes that

(1) there is complete diffusion in the liquid phase,
(2) there is local equilibrium at the solid-liquid interface,
(3) the equilibrium partition coefficient of solute elements applies at the solid-liquid interface and is constant throughout solidification,
(4) nucleation undercooling effects are negligible, and
(5) fluid-flow effects are negligible.

A. *Secondary-Dendrite-Arm-Spacing Model*

In the present model, the length scale in Eq. [6] is the final secondary dendrite arm spacing, which varies with cooling conditions and alloy composition. Using λ_{SDAS} values measured by several different researchers[47–51] at various cooling rates and steel carbon contents, an empirical relationship was obtained by a best fit as follows:

$$\begin{aligned}\lambda_{SDAS}\ (\mu m) &= (169.1 - 720.9 \cdot C_C) \cdot C_R^{-0.4935} \\ &\quad \text{for } 0 < C_C \le 0.15 \\ &= 143.9 \cdot C_R^{-0.3616} \cdot C_C^{(0.5501 - 1.996 \cdot \text{pct}C_C)} \\ &\quad \text{for } 0.15 < C_C\end{aligned} \quad [12]$$

where C_R is the cooling rate (°C/s) and C_C is the carbon content (wt pct C). Figure 1 compares the predicted and measured λ_{SDAS} as a function of carbon content at various cooling rates. The λ_{SDAS} value decreases steeply with increasing carbon content from zero to its minimum value at 0.15 wt pct C and then increases with increasing carbon content until about 0.6 wt pct C. From 0.6 to 1.0 wt pct C, λ_{SDAS} reduces again with increasing carbon content. This complicated variation of λ_{SDAS} with carbon content has been noted by other investigators.[47,52,53] El-Bealy and Thomas[52] suggested that this is because different solidification modes control the evolution of structure. Jacobi and Wünnenberg[47] reported that λ_{SDAS} decreases with increasing carbon content

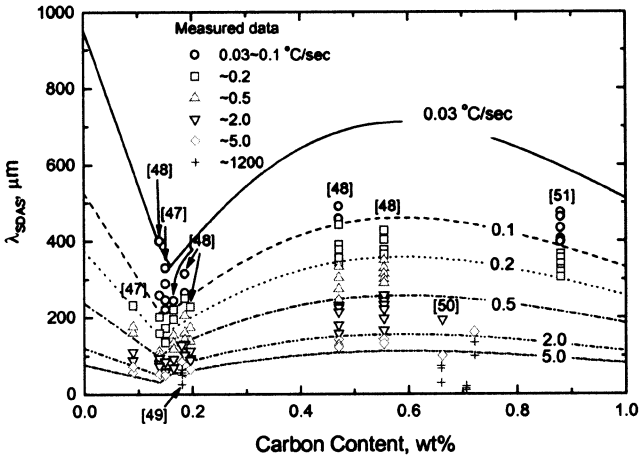

Fig. 1—Comparison of the predicted and measured secondary dendrite arm spacings[47–51] as a function of carbon content at various cooling rates.

during primary solidification of δ ferrite. When solidification starts with the γ phase, the effect of carbon content is not clear, because only two such alloys (0.59 and 1.48 wt pct C) were studied. It appears that λ_{SDAS} decreases with increasing cooling rate for all steels, as shown in Figure 1. At various cooling rates and carbon contents, the λ_{SDAS} values predicted with Eq. [12] are in reasonable agreement with the previous experimentally measured data.[47–51]

B. *Multicomponent-Alloy Effect*

In order to extend the model to multicomponent alloys, the effects of all individual components are summed. Mutual interaction effects between the alloying components on microsegregation are neglected. For each component, microsegregation is computed according to Eqs. [3], [5], [6], and [11], using appropriate values for the partition coefficients (k_i) and diffusion coefficients ($D_{S,i}$). The liquidus temperature (T_{liq}) depends on steel composition as follows:[39]

$$T_{liq} = T_{pure} - \sum_i m_i \cdot C_{0,i} \qquad [13]$$

where T_{pure} is the melting point of pure iron (1536 °C) and m_i is the slope of the liquidus line of each solute element in the pseudobinary Fe-phase diagram, given in Table I.[39] The temperature (T_{int}) that corresponds to a given interface composition in the liquid ($C_{L,i}$) is found by summing the contributions of all alloying elements (indicated by subscript i):

$$T_{int} = T_{pure} - \sum_i m_i \cdot C_{L,i} \qquad [14]$$

where k_i is the equilibrium partition coefficient of each solute element given in Table I, and $C_{L,i}$ depends on f_S according to Eqs. [3], [5], [6], and [11]. The solidus temperature is given when $f_S = 1.0$. The equilibrium solidus temperature can be calculated using the Lever rule (Eqs. [1] and [14]).

C. *Peritectic Phase-Transformation Effect*

In the equilibrium Fe-C phase diagram, two solid phases occur naturally: the δ-ferrite phase and the γ-austenite phase. For carbon contents lower than 0.53 wt pct, when the melt cools down slightly below the liquidus temperature, solid nucleates and grows as δ phase until solidification is complete (low carbon content) or until the peritectic temperature is reached (middle carbon content). At the peritectic temperature, solid γ phase starts to form around the periphery of the δ-phase dendrites, where the carbon content is higher. For carbon contents over 0.53 wt pct, the solid nucleates from the melt as γ phase, which grows until the end of solidification. These behaviors have important consequences on the metal properties that control microsegregation, as shown in Table I. The equilibrium partition coefficients, diffusion coefficients, and liquidus-line slopes of the solute elements depend greatly on the phase, according to measurements[40,41] and extrapolations[39,42,43] from the Fe-i (i = C, Si, Mn, P, and S) binary systems. The enrichment of solute elements in the interdendritic region during solidification causes a switch from δ-phase to γ-phase solidification once the carbon concentration exceeds 0.53 wt pct C. This change suddenly lowers the diffusion rates, which increases microsegregation and further lowers the solidus temperature.

In order to incorporate the δ/γ transformation into the present model, the peritectic starting temperature ($T^{\delta/\gamma}_{start}$ is needed. The δ/γ transformation is assumed to start when T_{int} in Eq. [14] drops to the local peritectic temperature ($T_{Ar4}(C_L)$), found using the partition coefficients and diffusion coefficient of the δ phase, according to

$$T^{\delta/\gamma}_{start} = T_{Ar4}(C_L) = T^{\delta/\gamma}_{pure} - \sum_i n_i \cdot k_i^{\delta/L} \cdot C^{\delta}_{L,i} \qquad [15]$$

where $T^{\delta/\gamma}_{pure}$ is the temperature of the δ/γ transformation of pure iron (1392 °C), n_i is the slope of the T_{Ar4} line of each solute element in its pseudobinary Fe-phase diagram (given in Table I[42]), $k_i^{\delta/L}$ is the equilibrium partition coefficient of each solute element i of the δ phase, and $C^{\delta}_{L,i}$ is the concentration of each solute element i at the liquid-solid δ-phase interface. Evaluating Eq. [15] at the initial liquid composition gives $T_{Ar4}(C_0)$:

$$T_{Ar4}(C_0) = T^{\delta/\gamma}_{pure} - \sum_i n_i \cdot k_i^{\delta/L} \cdot C^{\delta}_{0,i} \qquad [16]$$

The peritectic transformation is assumed to be controlled

Table I. Equilibrium Partition Coefficients, Diffusion Coefficients, and Liquidus Line Slopes of the Solute Elements[39–43]

Element	$k^{\delta/L}$	$k^{\gamma/L}$	D^{δ} (cm²/s)	D^{γ} (cm²/s)	m (°C/pct)	n (°C/pct)
C	0.19	0.34	0.0127 exp (−19,450/RT)	0.0761 exp (−32,160/RT)	78.0	−1122
Si	0.77	0.52	8.0 exp (−59,500/RT)	0.3 exp (−60,100/RT)	7.6	60
Mn	0.76	0.78	0.76 exp (−53,640/RT)	0.055 exp (−59,600/RT)	4.9	−12
P	0.23	0.13	2.9 exp (−55,000/RT)	0.01 exp (−43,700/RT)	34.4	140
S	0.05	0.035	4.56 exp (−51,300/RT)	2.4 exp (−53,400/RT)	38.0	160

Notes: R is gas constant of 1.987 cal/mol K, and T is temperature in Kelvin.

only by the carbon concentration at the solid-liquid interface. The δ/γ transformation is assumed to be complete when the carbon concentration at the liquid-solid interface becomes equal to 0.53 wt pct C, based on Eqs. [3], [5], [6], and [11] with the diffusion coefficients (D_i^{γ}) and partition coefficients ($k_i^{\gamma/L}$) of the γ phase. The corresponding carbon concentration in the solid phase is the triple point of the peritectic reaction in the equilibrium Fe-C binary-phase diagram.[54]

The δ fraction of the solid phase is assumed to decrease parabollically from 1, at the start of the δ/γ transformation, to zero at the end, according to

$$ {}^{\delta}f_S = \left(\frac{f_{\text{end}}^{\delta/\gamma} - f_S}{f_{\text{end}}^{\delta/\gamma} - f_{\text{start}}^{\delta/\gamma}} \right)^2 \cdot f_S \qquad [17] $$

If solidification is complete ($f_S = 1$) before the peritectic transformation is complete, ($C_C \geq 0.53$ pct), then Eq. [17] cannot be evaluated. Instead, the δ-phase solid fraction (${}^{\delta}f_S$) is found from a temperature form of this equation:

$$ {}^{\delta}f_S = \left(\frac{T_{\text{int}} - T_{Ar4}(C_0)}{T_{\text{start}}^{\delta/\gamma} - T_{Ar4}(C_0)} \right)^2 \cdot f_S \qquad [18] $$

where T_{int} and $T_{Ar4}(C_0)$ are found from Eqs. [14] and [16], respectively. Here, $T_{\text{start}}^{\delta/\gamma}$ is evaluated with Eq. [15] at the start of the peritectic transformation, $f_S = f_{\text{start}}^{\delta/\gamma}$, which is found when T_{int} equal $T_{\text{start}}^{\delta/\gamma}$, basing C_L on δ properties.

When the temperature is above $T_{\text{start}}^{\delta/\gamma}$ (*i.e.*, before the δ/γ transformation), the solid fraction is entirely δ phase ($f_S = {}^{\delta}f_S$). After the δ/γ transformation is complete, ${}^{\delta}f_S$ is zero. The remainder of the solid fraction is, naturally, γ phase.

$$ {}^{\gamma}f_S = f_S - {}^{\delta}f_S \qquad [19] $$

Equations [18] and [19] are needed to evaluate the average liquid concentrations ($C_{L,i}^{\text{ave}}$) needed in Eq. [14].

$$ C_{L,i}^{\text{ave}} = \frac{{}^{\delta}f_S}{f_S} \cdot C_{L,i}^{\delta} + \frac{{}^{\gamma}f_S}{f_S} \cdot C_{L,i}^{\gamma} \qquad [20] $$

This equation is needed to evaluate T_{int} when both the δ and γ phases are present.

D. *Cooling-History Effect*

The local solidification time (t_f) needed in Eq. [5] is found from the cooling history. For the constant cooling rate assumed in the present work, this simplifies to

$$ t_f = \frac{T_{\text{liq}} - T_{\text{sol}}}{C_R} \qquad [21] $$

E. *Solution Procedure*

A first estimate of the local solidification time is chosen by evaluating the equilibrium liquidus and solidus temperatures from Eq. [13] and the Lever rule (Eqs. [1] and [14]), respectively. From this initial guess, the value of T_{sol} is improved with a few iterative steps through Eqs. [12], [6], [21], [5], [11], [3], and [14] with $f_S = 1$, until consistent values are found for t_f, $C_{L,i}$, and $T_{\text{int}} = T_{\text{sol}}$.

If T_{int} in Eq. [14] is greater than $T_{Ar4}(C_L)$ in Eq. [15] when $f_s = 1$, then δ-phase properties are used in the previous procedure. If T_{liq} in Eq. [13] is less than $T_{Ar4}(C_0)$ in Eq. [16] when $f_s = 0$, or $C_{L,c}$ for γ is greater than 0.53 pct when $f_s = 1$, then γ-phase properties are used throughout. If none of these conditions are met, then both phases may exist, so the procedure is repeated for each of the γ and δ phases, and Eqs. [18] through [20] are then used to transform the separate sets of $C_{L,i}$ values to the single set of $C_{L,i}^{\text{ave}}$ values needed in Eq. [14].

After finding T_{sol}, the previous procedure can be repeated to find T_{int} for any other desired f_s value without the need for further iteration. In practice, it is often desirable to find the entire solid fraction and temperature relationship. Thus, it is convenient to solve these equations simply by trial and error by systematically incrementing the solid fraction from 0 to 1 in steps of 0.001.

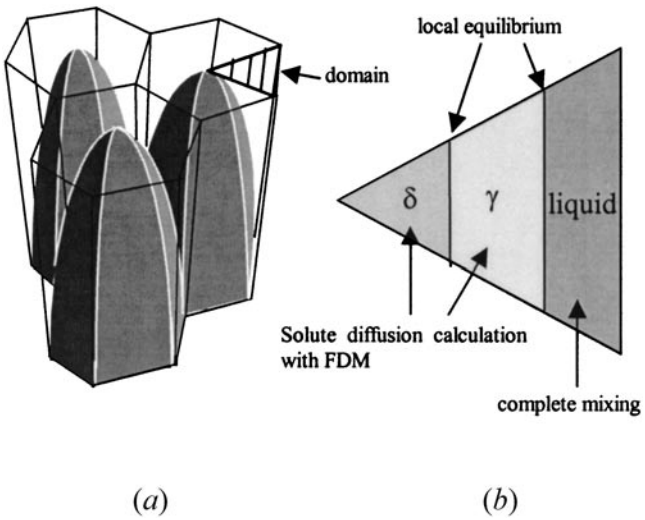

Fig. 2—(*a*) Schematic of the dendrite array morphology and (*b*) the corresponding transverse cross section assumed in the finite-difference simulation.

IV. FINITE-DIFFERENCE MODEL

In order to help validate the present simple model, a one-dimensional direct finite-difference model, based on that of Ueshima *et al.*,[18] was developed and implemented to track the liquid fraction, δ-phase solid fraction, and γ-phase solid fraction (${}^{\gamma}f_S$) in the mushy zone as a function of temperature and to calculate the solute redistribution. This model solves the following diffusion equations in a hexagonal domain chosen to approximate the morphology of columnar dendrites, as shown in Figure 2.

$$ \frac{\partial C_{S,i}}{\partial t} = \frac{\partial}{\partial x} \left(D_{S,i}(T) \frac{\partial C_{S,i}}{\partial x} \right) \qquad [22] $$

Complete mixing of solute elements in the liquid phase and local equilibrium at the liquid/δ, liquid/γ, and δ/γ interfaces are assumed. Diffusion of solute along the axial direction of the dendrite is assumed to be negligible. Thus, the model ignores macrosegregation due to fluid flow. As for the simple model, the equilibrium partition coefficients, diffusion coefficients, and slope of the liquidus line of the solute elements are given in Table I. The secondary dendrite arm spacings used in this study are given in Eq. [12] as functions of the cooling rate and carbon content. The calculation was made by dividing the triangular transverse cross

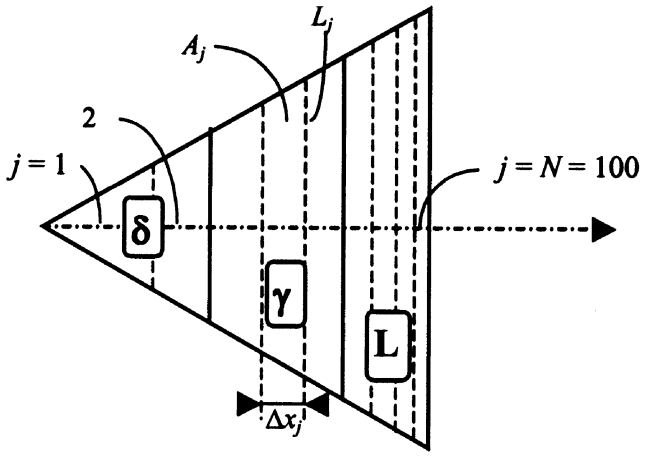

Fig. 3—Numerical discretization of the dendrite section for the finite-difference model domain.

section into 100 thin nodal areas, as shown in Figure 3. The domain size ($\lambda_{SDAS}/2$) is constant, so coarsening is ignored. The initial and boundary conditions are as follows.

Initial condition:

$$C_{S,i} = k^{S/L} \cdot C_{0,i} \text{ at } t = 0 \qquad [23]$$

Boundary condition:

$$\frac{\partial C_{S,i}}{\partial x} = 0 \text{ at } x = 0,\ \lambda_{SDAS}/2$$

When the liquidus temperature (T_{liq}) and the δ/γ transformation temperature, T_{Ar4} become equal to the actual temperature of a given nodal area, the solidification and δ/γ transformation in that area are assumed to be complete, and the interfaces move to the adjacent area. The parameters T_{liq} and T_{Ar4} are calculated using Eqs. [13] and [15], respectively. Further information on this model is presented elsewhere.[17–20]

V. MODEL VALIDATION

To assess the validity of the new simple model, the microsegregation predictions were compared with previous microsegregation results in three different systems, for which measurements and/or numerical solutions were available.

A. *Eutectic Formation in Aluminum Alloys*

The first test is for an aluminum alloy with 4.9 pct Cu, where the final eutectic volume fraction was measured.[21,55] A eutectic fraction prediction is readily obtained from Eqs. [3], [5], [6], and [11] of the simple model on setting C_L = 33.2 pct Cu for this binary system. Figure 4 compares the predicted eutectic volume fraction of the simple model as a function of cooling rate (or solidification time) with the experimental measurements of Sarreal and Abbaschian[21] and the numerical prediction by Voller and Beckermann[8] for the conditions of $k = 0.145$,[36] D_S (cm^2/s) $= 5 \cdot 10^{-9}$,[8] λ_{SDAS} (μm) $= 46.6 \cdot C_R^{-0.29}$, [21] and T_{liq} (°C) $= 660 - 3.374 \cdot$(pct Cu) for this binary system. The measured eutectic

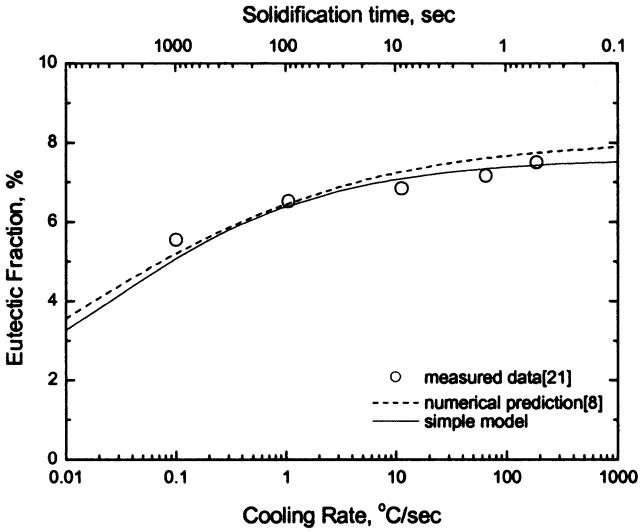

Fig. 4—Eutectic fraction (Al-4.9 pct Cu alloy in Table II) predicted with the simple model compared with experimental measurements[21] and the numerical prediction by Voller and Beckermann[8].

Table II. Data for Al-4.9 pct Cu Alloy Experiments[21]

C_R (°C/s)	t_f (s)	λ_{SDAS} (μm)	Eutectic Fraction (pct)
0.1	980	91	5.54
1.05	93.3	46	6.52
11.25	8.72	23	6.84
65	1.51	14	7.16
187	0.52	10	7.50

volume fractions[21] are given in Table II, based on conversions from the measured nonequilibrium second phase.[55] The predicted eutectic fractions from the simple model are in reasonable agreement with these measurements.

B. *Segregation in Liquid Steel*

The second validation of the simple model investigated microsegregation of manganese and carbon for steel M1 in Table III. For this test, the manganese concentration predicted by the simple model was compared with the results of the complete finite-difference model (Section IV) and other simple models, including the Lever rule in Eq. [1], the Scheil Eq. [2], and the different forms of Eq. [3], including the equations of Brody–Flemings (Eq. [4]), Ohnaka (Eqs. [7] and [8]), and Clyne–Kurz (Eq. [9]). The results are compared in Figure 5 for assumed conditions of X = 180 μm, $D_S = 1.378 \cdot 10^{-7}$ cm^2/s, t_f = 879.2 seconds, k = 0.77, and C_0 = 1.52, based on the property data in Table I. The simple model is in good agreement with the present finite-difference model. The Brody–Fleming equation and Ohnaka equation (Eq. [8]) also predict nearly the same microsegregation. However, the original Clyne–Kurz equation and the Ohnaka equation (Eq. [7]) predict slightly higher microsegregation, with almost identical values, as shown in Table IV.

Figure 6 compares the changes of the carbon concentration in the liquid phase at the solid-liquid interface. For the

Table III. Chemical Compositions of Carbon Steels (Weight Percent) and Cooling Rates (°C/s)

Sample	C	Si	Mn	P	S	C_R	Reference
M1	0.13	0.35	1.52	0.016	0.002	0.045, 0.25	17
S1	0.06 to 0.6	0.015	1.05	0.0009	0.0008	0.17	22
S2	0.12 to 0.81	0.24	0.61	0.015	0.009	1	23
S3	0.015 to 1.0	0.34	1.52	0.012	0.015	10	24

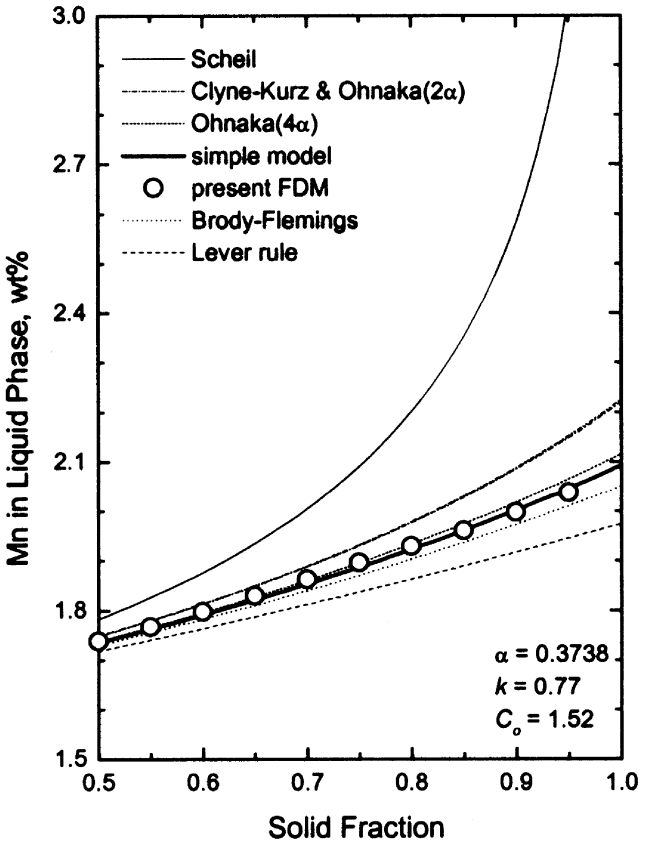

Fig. 5—Comparison of manganese concentration in the liquid calculated by various simple equations with the present finite-difference model results (0.13 pct C steel M1 in Table III).

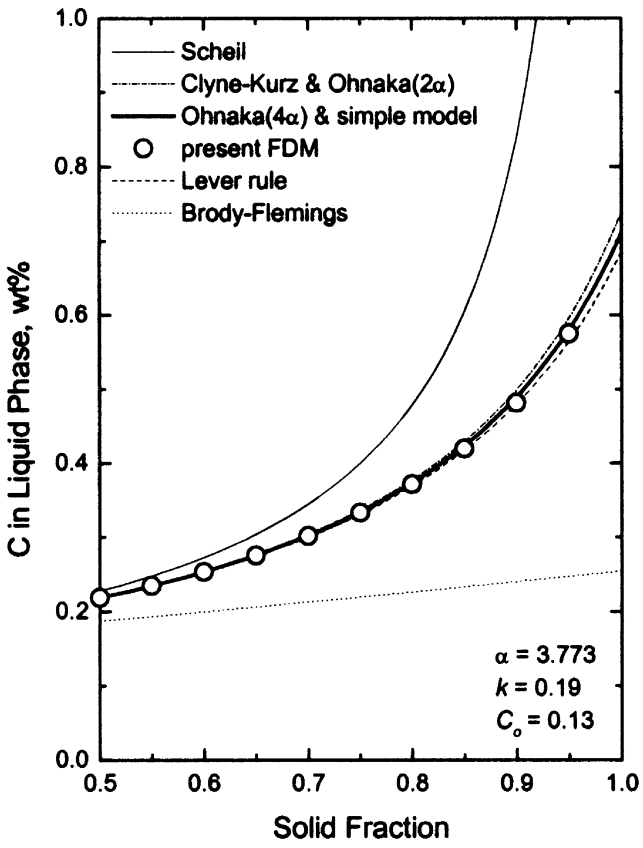

Fig. 6—Comparison of carbon concentration in the liquid calculated by various simple equations with the present finite-difference model results (0.13 pct C steel M1 in Table III).

Table IV. Different Microsegregation Equation Predictions of β for Two Sets of Conditions (α Values)

	β						
α	Eq. [1]	Eq. [2]	Eq. [4]	Eq. [7]	Eq. [8]	Eq. [9]	Eq. [11]
0.3738	1	0	0.7476	0.4278	0.5992	0.4336	0.6455
3.773	1	0	7.546	0.8830	0.9376	0.8810	0.9388

conditions of $X = 180$ μm, $D_S = 7.263 \cdot 10^{-6}$ cm^2/s, $t_f =$ 168.3 seconds, $k = 0.19$, and $C_0 = 0.13$, all equations except the Scheil and Brody–Fleming equations predict almost the same microsegregation. As Clyne and Kurz[34] explained, when α is large, the Brody–Flemings equation predicts less enrichment in the liquid phase than does the Lever rule, so it is physically unreasonable. The Scheil equation naturally overpredicts the enrichment. The other models predict similar large β values, so their liquid-concentration predictions are similar, as shown in Table IV. Even the Lever rule ($\beta = 1$) is quite reasonable, as carbon diffusion is almost complete for the large value of α in this problem (3.773). In summary, the liquid concentrations of the present simple model agree well for a wide range of α values, as shown in Figures 4 through 6.

For the next validation test, model predictions are compared with the experimental measurements by Matsumiya *et al.*[17] for steel M1, which was solidified unidirectionally and quenched with a columnar structure at two different cooling rates. The measured primary dendrite arm spacing

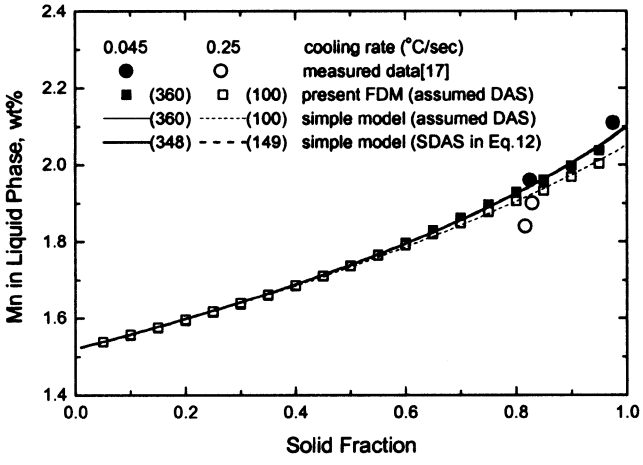

(*a*)

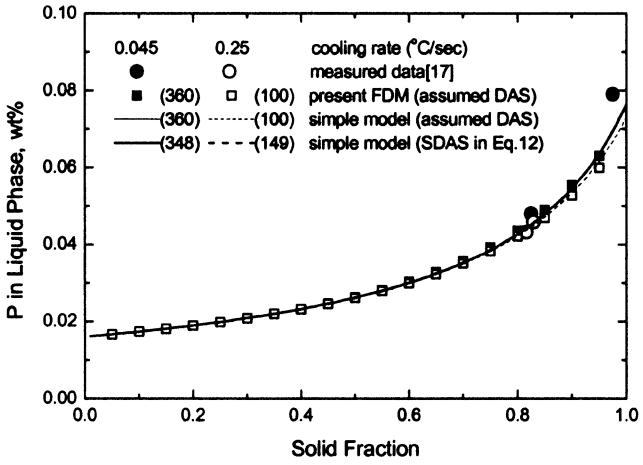

(*b*)

Fig. 7—Comparison of the calculated (*a*) manganese and (*b*) phosphorus concentration in the liquid phase and experimental measurements[17] (0.13 pct C steel M1 in Table III).

was 360 μm at cooling rates of 0.045 °C/s and 0.25 °C/s. The secondary dendrite arm spacing was 100 μm at 0.25 °C/s. But, at 0.045 °C/s, the dendrites in the microstructure did not exhibit clear patterns for secondary dendrite arm spacing. Although it is not exactly clear, the measurement appears to be some average of the solute concentration in the quenched region, including both interdendritic primary-arm and interdendritic secondary-arm material. Accordingly, calculations were performed with both microsegregation models for the primary arm spacing of 360 μm at 0.045 °C/s and for the secondary arm spacing of 100 μm at 0.25 °C/s. Calculations were also performed using the secondary dendrite arm spacing obtained from Eq. [12].

Figure 7 compares the calculated manganese and phosphorus concentrations in the liquid phase at the solid-liquid interface. All calculations fall between the experimental measurements for both cooling rates, as shown in Figure 7. The results using spacings from Eq. [12] are almost identical for both cooling rates, as 0.045 °C/s with the primary dendrite arm spacing of 360 μm. This is because the parameter t_f/X^2 is about the same, as shown in Table V. The relative accuracy of all of these similar predictions could not be resolved within the experimental uncertainly.

Table V. Variation of Parameter t_f/X^2 at Conditions for Steel M1 (Table III)

	Asssumed DAS		δ_{SDAS} in Eq. [12]	
C_R (°C/s)	0.045	0.25	0.045	0.25
X (μm)	180	50	174	74.5
t_f (s)	879.2	143.9	835.5	150.6
t_f/X^2 ($\times 10^{-2}$ s/μm^2)	2.714	5.756	2.760	2.713

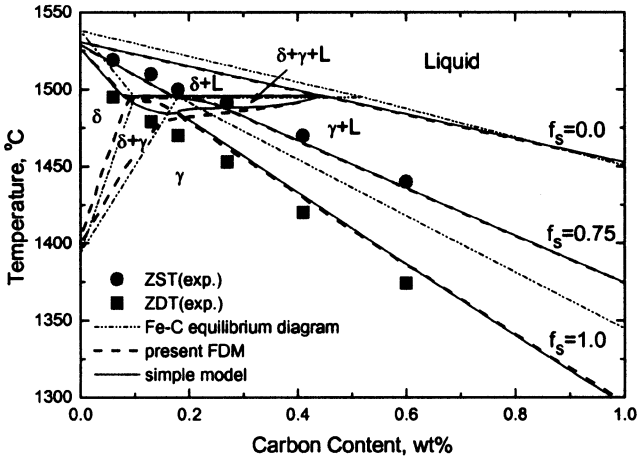

Fig. 8—Nonequilibrium pseudobinary Fe-C phase diagram of 0.015Si-1.05Mn-0.0009P-0.0008S carbon steels at a cooling rate of 0.17 °C/s, compared with ZST and ZDT measurements.[22]

C. *Solidification Temperatures of Steel*

The final three validation tests focus on the nonequilibrium 75 pct solid and solidus temperatures for three different steel systems at three different cooling rates. These two solid fractions are chosen because they are believed[20] to correlate with the sudden mechanical-property changes observed during high-temperature tensile tests with *in-situ* melting.[22–26] Specifically, these measurements have identified a zero-strength temperature (ZST) and a zero-ductility temperature (ZDT). Above the ZST, solidifying steel has no strength and no ductility and behaves as a liquid. At temperatures between the ZST and ZDT, the steel has no ductility, but does have some strength due to the mechanical network between dendrites. As long as some liquid remains, the steel fails in a brittle manner due to a rapid strain concentration and failure of the interdendritic liquid film. Below the ZDT, the solidifying steel behaves as a solid with both strength and ductility.

The ZDT should, theoretically, be found at the nonequilibrium solidus temperature, where the solid fraction approaches 1. Won *et al.*[20] reported that the critical solid fraction at ZST corresponds to 0.75, based on a statistical assessment of microsegregation measurements and a finite-difference model at various carbon contents and cooling rates.

Nonequilibrium pseudo Fe-C phase diagrams are calculated using both the simple model and the present finite-difference model and are compared with ZST and ZDT measurements[22,23,24] in Figures 8 through 10. The experiments were performed by melting steel samples in a quartz tube and conducting tensile tests on the solidifying steel

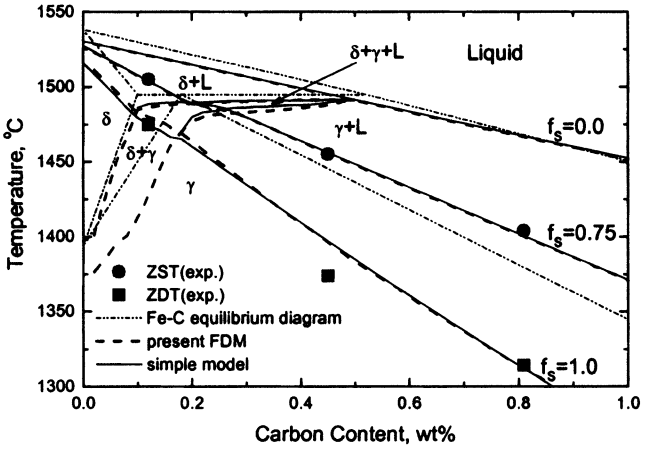

Fig. 9—Nonequilibrium pseudobinary Fe-C phase diagram of 0.24Si-0.61Mn-0.015P-0.009S carbon steels at a cooling rate of 1 °C/s, compared with ZST and ZDT measurements.[23]

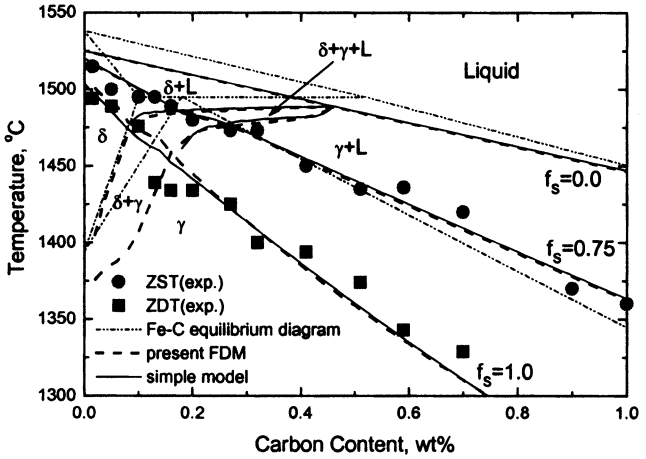

Fig. 10—Nonequilibrium pseudobinary Fe-C phase diagram of 0.34Si-1.52Mn-0.012P-0.015S carbon steels at a cooling rate of 10 °C/s, compared with ZST and ZDT measurements.[24]

using a Gleeble system. For the calculations, the length scale was calculated using λ_{SDAS} from Eq. [12], and the steel compositions are given in Table III.

The nonequilibrium phase diagram in Figure 8 is calculated for steel S1 and compared with the ZST and ZDT measurements of Shin *et al.*[22] at a cooling rate of 0.17 °C/s and a strain rate of 0.01 s^{-1}. The calculated ZDT is only 1.24 °C to 4.24 °C below the equilibrium solidus temperature, as shown in Table VI. Figure 9 is based on steel S2 for the ZST and ZDT measurements of Seol *et al.*[23] at 1.0 °C/s and 0.01 s^{-1}. The calculated undercooling of the ZDT below the equilibrium solidus temperature increases from 2.65 °C to 17.25 °C with increasing C content. Figure 10 is based on steel S3 and is compared with the measurements of Schmidtmann and Rekoski[24] at 10 °C/s and 0.2 s^{-1}. The calculated undercooling of the ZDT increases from 3.73 °C to 31.09 °C with increasing carbon content, as shown in Table VI.

The extent of segregation-related undercooling of the final solidification temperature (ZDT) increases both with increasing carbon content and with increasing alloy content from steels S1 (Figure 8) to S2 (Figure 9) to S3 (Figure 10). Increasing the carbon content extends the mushy zone. More importantly, the liquid concentration can exceed 0.53 pct C more easily, so γ phase is more likely to form during solidification. For carbon contents less than about 0.1 wt pct, the δ/γ transformation takes place after solidification, so segregation undercooling is small. With greater carbon contents, some γ phase forms during solidification. Diffusion through the closer-packed austenite structure is slower, so microsegregation increases and depresses the solidus temperature further below equilibrium. In particular, the segregation of S and P becomes increasingly important with an increased freezing range and austenite fraction. This is because these elements also have very low partition coefficients, which are even smaller for the γ phase than for the δ phase. Finally, the increasing depression of the solidus temperature from steels S1 to S2 to S3 is also caused, in part, by the increasing cooling rate for these three case studies.

In all three Figures 8 through 10, the measured ZST and ZDT data roughly agree with the calculated temperatures at which the solid fraction becomes 0.75 and 1.0, respectively. The results of the simple model also agree with those of the finite-difference model. The slight discrepancy for 0.1 to 0.2 wt pct C steels is because the simple model does not account for the diffusion between solid phases that affects the peritectic reaction. Even so, the calculated starting temperature and ending temperature of the δ/γ transformation roughly agree between the two models.

Figure 11 compares predictions of the simple microsegregation model with the experimentally measured liquidus,[27–30] solidus,[27–30] peritectic temperatures, [27,28,29] ZST,[22–24,26] and ZDT.[22–26] The liquidus, solidus, and peritectic temperatures were obtained by differential thermal analysis (DTA) at a range of slow cooling rates.[27–30] All calculations are in reasonable agreement with the measurements, although there is more scatter in the solidus temperature predictions. The ZST and ZDT measurements[22–26] agree well with the predictions, as discussed previously. In summary, these test results show that the proposed simple

Table VI. Calculated Solidus Temperature Using the Lever Rule and Simple Model for Steels S1, S2, and S3 (Table III Conditions)

	0.044 Wt Pct C		0.18 Wt Pct C		0.8 Wt Pct C	
Sample	Lever Rule	Simple Model	Lever Rule	Simple Model	Lever Rule	Simple Model
S1	1510.28 (°C)	1509.04	1486.78	1484.88	1344.55	1340.31
S2	1502.55	1499.90	1473.63	1465.28	1331.39	1314.14
S3	1491.59	1487.86	1460.73	1447.13	1318.49	1287.40

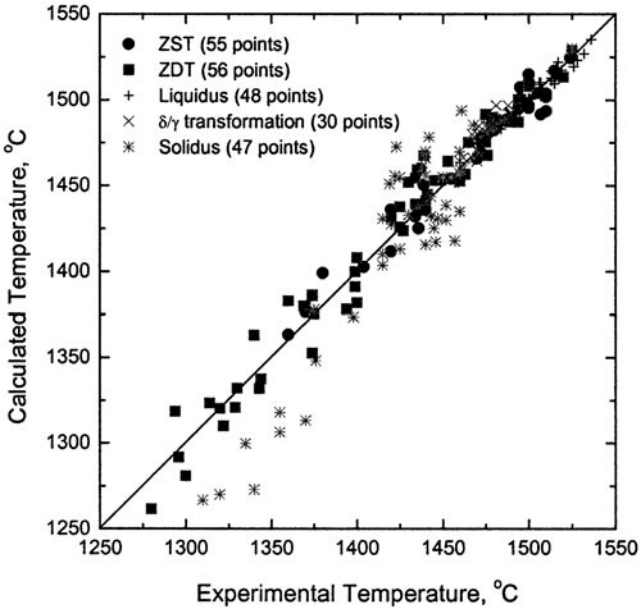

Fig. 11—Calculated *vs* experimental liquidus,[27–30] solidus,[27–30] peritectic temperatures,[27–29] ZST,[22–24,26] and ZDT [22–26] in plain carbon steels.

microsegregation model can reasonably simulate a range of solidification phenomena, especially for steel.

D. *Discussion*

The solidus temperature measured by DTA is generally greater than the measured ZDT for the same conditions, especially for a high carbon content.[56,57] This is because the DTA measurement has difficulty detecting the solidification of the last few percentages of liquid,[56] which is found segregated at the grain boundaries and governs the ZDT. The present model assumes that these two temperatures are the same and better predicts the ZDT, so solidus temperatures are naturally underestimated in high-carbon steels, as shown in Figure 11. The model, thus, appears to empirically incorporate both interdendritic and grain-boundary segregation. A more sophisticated model might simulate both interdendritic microsegregation and macrosegregation at the grain-size scale to account for the differences between grain-boundary and interdendritic liquid. Such a model could resolve the apparent discrepancy by matching both measurements. Further research is needed with both modeling and measurements in order to quantify the behavior of alloys in steel during the final stages of solidification.

VI. EFFECTS OF COOLING RATE AND SECONDARY DENDRITE ARM SPACING

The present simple microsegregation model was next applied to investigate the effects of cooling rate and secondary dendrite arm spacing on microsegregation for the three steel compositions of 0.044, 0.18, and 0.8 wt pct C with 0.34 pct Si-1.52 pct Mn-0.012 pct P-0.015 pct S (*i.e.*, based on steel S3 in Table III). To isolate the effect of cooling rate alone on microsegregation, the secondary dendrite arm spacings are first assumed to be constants of 44.1, 45.1, and 79.0 μm for carbon contents of 0.044, 0.18, and 0.8 wt pct

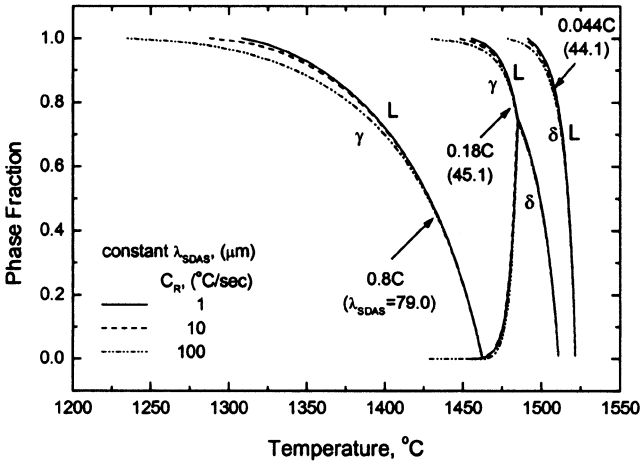

Fig. 12—Effect of cooling rate on phase fraction evolution for three different steels calculated with the simple model.

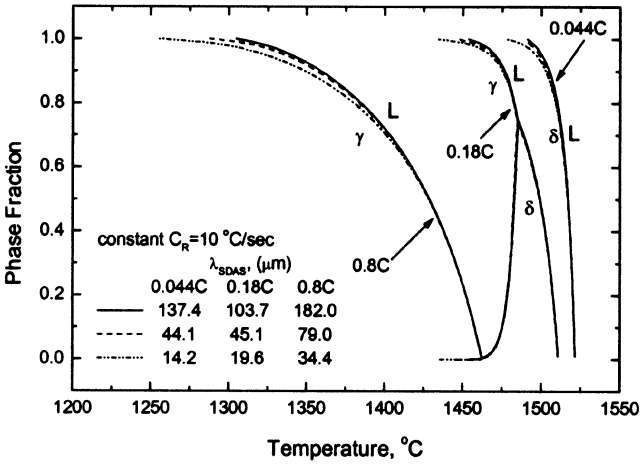

Fig. 13—Effect of secondary dendrite arm spacing on phase fraction evolution for three different steels calculated with the simple model.

C, respectively. Figure 12 shows the phase-fraction results calculated with the present model as a function of temperature. The calculated nonequilibrium solidus temperature for all three steels decreases with increasing cooling rate from 1 °C/s to 100 °C/s. The extent of the decrease increases from 3 °C to 74 °C for alloy contents increasing from 0.044 to 0.8 wt pct C.

To isolate the effect of length scale alone on microsegregation, the cooling rate is fixed at 10 °C/s for three different secondary dendrite arm spacings. Figure 13 shows the evolution of the phase fractions for the various spacings and steel compositions. The calculated nonequilibrium solidus temperature decreases slightly with increasing secondary dendrite arm spacing. The extent of the decrease increases from 12 °C to 50 °C for alloy contents increasing from 0.044 to 0.8 wt pct C.

The solidus temperature has just been shown to decrease with both increasing cooling rate and increasing secondary dendrite arm spacing. In real casting processes, the secondary dendrite arm spacing itself evolves during solidification, specifically decreasing with increasing cooling rate. In the surface region, the secondary dendrite arm spacing is small,

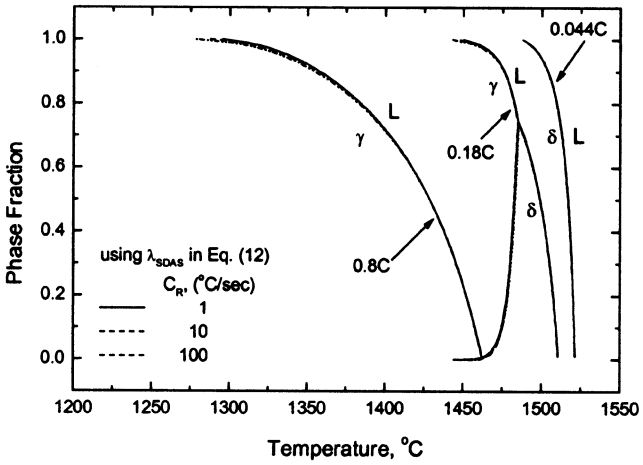

(*a*)

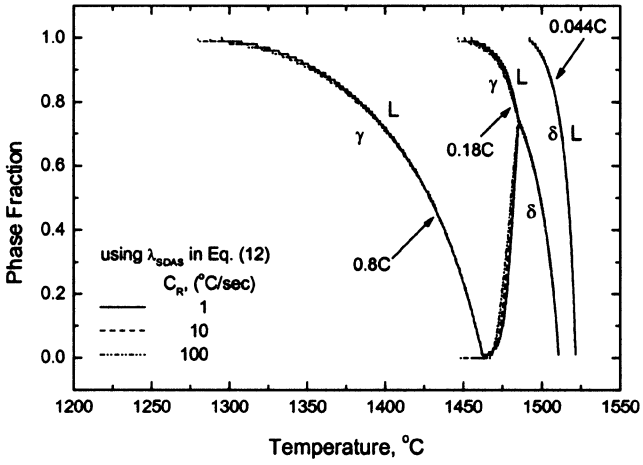

(*b*)

Fig. 14—Evolution of phase fractions with temperature during solidification for conditions in Table VI calculated with (*a*) the simple model and (*b*) the finite difference model.

Table VII. Calculated Secondary Dendrite Arm Spacings from Equation [12]

	λ_{SDAS} (μm)		
C_R (°C/s)	0.044 Wt Pct C	0.18 Wt Pct C	0.8 Wt Pct C
1	137.4	103.7	182.0
10	44.1	45.1	79.0
100	14.2	19.6	34.4

because the cooling rate is high due to the large heat extraction. In the interior, the secondary arm spacing is larger due to the slower cooling rate. Thus, the two opposite effects should partially cancel in a real casting.

In order to investigate the combined effects of cooling rate and secondary dendrite arm spacing, calculations were performed with both microsegregation models at the three cooling rates of 1 °C/s, 10 °C/s, and 100 °C/s using the secondary dendrite arm spacing obtained from Eq. [12]. Figure 14 shows the evolution of the phase fractions as a function of temperature for the conditions given in Table VII. As expected, the phase fractions calculated at 1 °C/s are nearly the same as those at 100 °C/s, because the secondary dendrite arm spacing decreases with increasing cooling rate. This shows that the decrease in solidus temperature caused by the increasing cooling rate is almost cancelled by the increase in solidus temperature accompanying the closer secondary dendrite arm spacing. For the 0.044 wt pct C steel, the solidus temperatures are the same within ±0.1 °C, as shown in Table VIII, part 3. For 0.18 and 0.8 wt pct C steels, the solidus temperatures still decrease by 7.6 °C and 17.9 °C, respectively, due to the combined effects of increasing the cooling rate from 1 °C/s to 100 °C/s. The effect of cooling rate is more important than that of secondary dendrite arm spacing, so the cancellation is not perfect. However, these small differences contrast with the 20 °C to 70 °C changes in solidus temperatures predicted with independent changes in the cooling rate or secondary dendrite arm spacing (Table VIII, parts 1 and 2).

This prediction that the overall effect of an increasing cooling rate is a slight decrease in solidus temperature is consistent with measurements. Quantitatively, the present model appears to underpredict the effect measured using DTA. Specifically, increasing the cooling rate from 0.1 °C/s to 2 °C/s decreased the measured solidus temperatures of several different steels by 10 °C to 35 °C,[27] while this work predicts a decrease of only 0 °C to 10 °C for the same conditions. However, measurements of the ZDT are much less sensitive to cooling rate. Seol *et al.*[23] determined that increasing the cooling rate from 1 °C/s to 10 °C/s decreased the measured ZDT by only 5 °C to 20 °C. This compares with the 0.1 °C to 8 °C decrease predicted here. Other work has even measured a slight increase in the ZDT with increasing cooling rate.[26,57] Thus, the present model appears to predict a reasonable compromise of ZDT measurements in the literature.

VII. NONEQUILIBRIUM PHASE DIAGRAM AND CRACK FORMATION

Figure 15 shows the nonequilibrium pseudo Fe-C phase diagram for steel S3 at cooling rates of 1 °C/s, 10 °C/s, and 100 °C/s using the present analytical model. The secondary dendrite arm spacings from Eq. [12] vary with both carbon content and cooling rate. For this model, the solid fractions of 0.0, 0.75, 0.9, and 1.0 are believed to correspond to the characteristic temperatures of T_{liq}, the ZST, the liquid impenetrable temperature (LIT), and the ZDT, respectively.

The ability to accurately predict these temperatures is of practical consequence to the prediction, understanding, and avoidance of cracks, such as hot tears. Cracks that form above the LIT are refilled with liquid fed in from the bulk. Cracks that form below the LIT cannot refill, however, because the dendrite arms are close enough to resist feeding of the liquid. This critical temperature is proposed to correspond to a solid fraction of 0.9.[19,58,59] Figure 15 shows that the combined effects of cooling rate and secondary dendrite arm spacing on T_{liq}, ZST, and LIT are not significant. However, the combined effects on the ZDT are significant in steels above 0.1 wt pct C with a high alloy content. This is due to the enhanced segregation of solute elements near the final stage of solidification and the lower partition coefficients for the γ phase, relative to the δ phase. With increasing carbon content, increasing the cooling rate lowers the ZDT more, which increases the critical temperature range between

Table VIII. Calculated Solidus Temperatures Using the Simple Model for Steel S3 (Table III)

	0.044 Wt Pct C		0.18 Wt Pct C		0.8 Wt Pct C	
C_R (°C/s)	λ_{SDAS} (μm)	T_{sol} (°C)	λ_{SDAS}	T_{sol}	λ_{SDAS}	T_{sol}
1. Constant secondary dendrite arm spacing						
1	44.1	1491.00	45.1	1455.64	79.0	1308.44
10	44.1	1487.86	45.1	1447.13	79.0	1287.40
100	44.1	1478.39	45.1	1428.13	79.0	1234.14
2. Constant cooling rate						
10	137.4	1478.55	130.7	1434.06	182.0	1254.72
10	44.1	1487.86	45.1	1447.13	79.0	1287.40
10	14.2	1490.99	19.6	1454.00	34.4	1304.75
3. Combined effects of cooling rate and secondary dendrite arm spacing						
1	137.4	1487.93	130.7	1450.38	182.0	1295.43
10	44.1	1487.86	45.1	1447.13	79.0	1287.40
100	14.2	1487.78	19.6	1442.83	34.4	1277.52

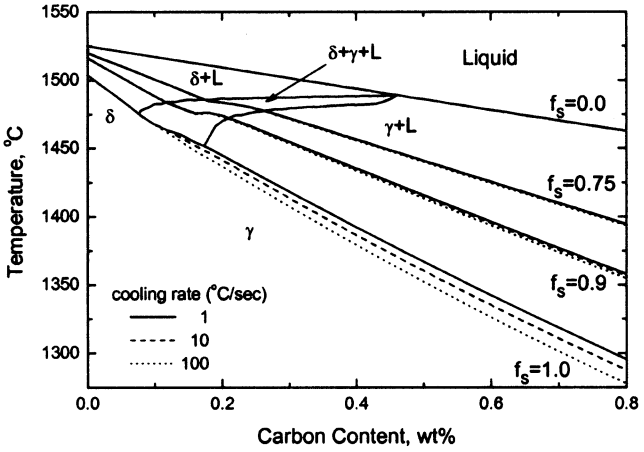

Fig. 15—Combined effects of cooling rate and secondary dendrite arm spacing (Eq. [12]) on T_{liq} (f_S = 0.0), ZST (f_s = 0.75), LIT (f_s = 0.9), and ZDT (f_s = 1.0) of steel S3 (in Table III) calculated with the simple microsegregation model.

the LIT and ZDT. This suggests that the tendency for cracking during solidification should increase with increasing cooling rate, with increasing carbon contents above 0.1 wt pct C, and with increasing alloy contents.

Further complexities arise due to flow and macrosegregation, nonuniform heat transfer, thermal-mechanical deformation, and stress concentration. Further work is needed to incorporate the simple model presented here into other advanced macroscopic models to simulate fluid flow, heat transfer, and stress during solidification processes.

VIII. CONCLUSIONS

A simple analytical model of microsegregation based on the Clyne–Kurz model has been developed, which takes into account the effects of multiple components, columnar dendrites, coarsening, and the δ/γ transformation for application to the solidification of steels. A new empirical equation for the secondary dendrite arm spacing, which varies with cooling rate and carbon content, has been proposed, based on measurements by several different researchers, as follows.

$$\lambda_{SDAS}\ (\mu m) = (169.1 - 720.9 \cdot C_C) \cdot C_R^{-0.4935} \quad \text{for } 0 < C_C \le 0.15$$

$$= 143.9 \cdot C_R^{-0.3616} \cdot C_C^{(0.5501 - 1.996 \cdot \text{pct}C_C)} \quad \text{for } 0.15 < C_C$$

Predictions with this microsegregation model agree with both experimental measurements and calculations with a detailed finite-difference model. Model predictions for a range of steel compositions, cooling rates, and secondary dendrite arm spacings reveal the following.

1. The solidus temperature is lowered significantly with independent increases in either the cooling rate or secondary dendrite arm spacing.
2. In real castings, where spacings change with cooling rate, the effect of cooling rates less than 100 °C/s on phase-fraction evolution is insignificant in low-alloy steels with less than 0.1 wt pct C and for phase fractions below 0.9 in other steels.
3. The solute-element concentration, especially phosphorus and sulfur, has a significant effect on the solidus temperature and ZDT, due to their enhanced segregation near the final stage of solidification.

The simple analytical model presented here can easily and efficiently incorporate microsegregation phenomena into solidification calculations for use in advanced macroscopic models.

ACKNOWLEDGMENTS

The authors thank the members of the Continuous Casting Consortium, University of Illinois, for support of this work, including Allegheny Ludlum (Brackenridge, PA), AK Steel (Middletown, OH), Columbus Stainless (South Africa), ISPAT–Inland Steel (East Chicago, IN), LTV Steel (Cleveland, OH), and Stollberg, Inc. (Niagara Falls, NY). Special thanks are due to Ya Meng for help with the fortran and spreadsheet implementations of the method.

NOMENCLATURE

C_C average carbon concentration (wt pct)
$C_{L,l}^{ave}$ average liquid concentration during the δ/γ transformation (wt pct)

C_L	liquid concentration (wt pct)
C_0	initial liquid concentration (wt pct)
C_R	cooling rate (°C/s)
D_S	diffusion coefficient (cm^2/s)
f_S	solid fraction
$f_{\text{end}}^{\delta/\gamma}$	ending solid fraction of δ/γ transformation
$f_{\text{start}}^{\delta/\gamma}$	starting solid fraction of δ/γ transformation
δ_{fs}	δ-phase fraction in the solid phase
γ_{fs}	γ-phase fraction in the solid phase
i	solute element (carbon, silicon, manganese, phosphorus, or sulfur)
k	equilibrium partition coefficient
m	slope of the liquidus line (°C/pct)
n	slope of the T_{Ar4} line (°C/pct)
T_{int}	interface temperature, Eq. [14] (°C)
T_{liq}	liquidus temperature, Eq. [13] (°C)
T_{pure}	melting point of pure iron (1536 °C)
T_{sol}	solidus temperature (°C)
T_{Ar4}	starting temperature of δ/γ transformation (°C)
$T_{\text{pure}}^{\delta/\gamma}$	temperature of δ/γ transformation of pure iron (1392 °C)
$T_{\text{start}}^{\delta/\gamma}$	starting temperature of δ/γ transformation (°C)
t	time (s)
t_f	local solidification time (s)
X	length scale of the microsegregation domain
x	width of the nodal area
α	Fourier number, Eq. [5]
α^+	Fourier number accounts for coarsening
α^C	extra back-diffusion from coarsening = 0.1
β	back-diffusion parameter
λ_{SDAS}	secondary dendrite arm spacing (μm)

REFERENCES

1. M.C. Flemings and G.E. Nereo: *Trans. TMS-AIME*, 1967, vol. 239. pp. 1449-61.
2. R. Mehrabian, M. Keane, and M.C. Flemings: *Metall. Trans.*, 1970, vol. 1, pp. 1209-20.
3. T. Fuji, D.R. Poirier, and M.C. Flemings: *Metall. Trans. B*, 1979, vol. 10B, pp. 331-39.
4. H. Mizukami, M. Komatsu, T. Kitagawa, and K. Kawakami: *Trans. Iron Steel Inst. Jpn.* 1984, vol. 24, pp. 940-49.
5. K.S. Oh, I.R. Lee, Y.K. Shin, Y.S. Koo, I.J. Lee, and D.Y. Lee: *Proc. 6th Int. Iron Steel Congr.*, ISIJ, Nagoya, 1990, pp. 256-63.
6. K. Ayata, S. Koyama, H. Nakata, S. Kawasaki, K. Ebina, and T. Hata: *Proc. 6th Int. Iron Steel Congr.*, ISIJ, Nagoya, 1990, pp. 279-84.
7. M. El-Bealy: *Scand. J. Metall.*, 1995, vol. 24, pp. 63-80.
8. V.R. Voller and C. Beckermann: *Metall. Mater. Trans. A*, 1999, vol. 30A, pp. 2183-89.
9. J. Miettinen: *Metall. Trans. A*, 1992, vol. 23A, pp. 1155-70.
10. C.Y. Wang and C. Beckermann: *Mater. Sci. Eng.*, 1993, vol. 171, pp. 199-211.
11. J.F. McCarthy: *Acta Mater.*, 1997, vol. 45, pp. 4077-91.
12. A. Karma and W.J. Rappel: *Phys. Rev. D*, vol. 57, pp. 4323-49.
13. J. Tiaden: *J. Cryst. Growth*, 1999, vol. 199, pp. 1275-80.
14. J.S. Lee, S.G. Kim, W.T. Kim, and T. Suzuki: *Iron Steel Inst. Jpn. Int.*, 1999, vol. 39, pp. 730-36.
15. B. Nestler and A.A. Wheeler: *Physica D*, 2000, vol. 138, pp. 114-33.
16. J. Rappaz and J.F. Scheid: *Math. Methods Appl. Sci.*, 2000, vol. 23, pp. 491-513.
17. T. Matsumiya, H. Kajioka, S. Mizoguchi, Y. Ueshima, and H. Esaka: *Trans. Iron Steel Inst. Jpn.*, 1984, vol. 24, pp. 873-82.
18. Y. Ueshima, S. Mizoguchi, T. Matsumiya, and H. Kajioka: *Metall. Trans. B*, 1986, vol. 17B, pp. 845-59.
19. K. Kim, T. Yeo, K.H. Oh, and D.N. Lee: *Iron Steel Inst. Jpn. Int.*, 1996, vol. 36, pp. 284-89.
20. Y.M. Won, K.H. Kim, T. Yeo, and K.H. Oh: *Iron Steel Inst. Jpn. Int.*, 1998, vol. 38, pp. 1093-99.
21. J.A. Sarreal and G.J. Abbaschian: *Metall. Trans. A*, 1984, vol. 17A, pp. 2063-73.
22. G. Shin, T. Kajitani, T. Suzuki, and T. Umeda: *Tetsu-to-Hagané*, 1992, vol. 78, pp. 587-93.
23. D.J. Seol, Y.M. Won, K.H. Oh, Y.C. Shin, and C.H. Yim: *Iron Steel Inst. Jpn. Int.*, 2000, vol. 40, pp. 356-63.
24. E. Schmidtmann and F. Rakoski: *Arch. Eisenhüttenwes.*, 1983, vol. 54, pp. 357-62.
25. H.G. Suzuki, S. Nishimura, and Y. Nakamura: *Trans. Iron Steel Inst. Jpn.*, 1984, vol. 24, pp. 54-59.
26. T. Nakagawa, T. Umeda, J. Murata, Y. Kamimura, and N. Niwa: *Iron Steel Inst. Jpn.*, 1995, vol. 35, pp. 723-29.
27. *A Guide to the Solidification of Steels*, Jernkontoret, Stockholm, 1977.
28. L. Ericson: *Scand. J. Metall.*, 1977, vol. 6, pp. 116-24.
29. S. Kobayashi: *Trans. Iron Steel Inst. Jpn.*, 1988, vol. 28, pp. 535-42.
30. Y.C. Shin, J. Choi, and C.H. Yim: Technical Report, Iron & Steel Making Research Team, Technical Research Labs., POSCO, Korea, 1998.
31. E. Scheil: *Z. Metallkd.*, 1942, vol. 34, pp. 70-72.
32. H.D. Brody and M.C. Flemings: *Trans. TMS-AIME*, 1966, vol. 236, pp. 615-24.
33. I. Ohnaka: *Trans. Iron Steel Inst. Jpn.*, 1986, vol. 26, pp. 1045-51.
34. T.W. Clyne and W. Kurz: *Metall. Trans. A*, 1981, vol. 12A, pp. 965-71.
35. S. Kobayashi: *J. Cryst. Growth*, 1988, vol. 88, pp. 87-96.
36. T.P. Battle and R.D. Pehlke: *Metall. Trans. B*, 1990, vol. 21B, pp. 357-75.
37. J. Miettinen: *Ironmaking and Steelmaking*, 1996, vol. 23, pp. 346-56.
38. J. Miettinen: *Metall. Mater. Trans. B*, 1997, vol. 28B, pp. 281-97.
39. T. Kawawa: *Tekko-no-Gyoko (Solidification of Steel)*, Solidification Comm. of ISIJ, ISIJ, Tokyo, 1977, Appendix 13.
40. Y. Nakamura and H. Esaka: *Tetsu-to-Hagané*, 1981, vol. 67, p. S140.
41. *Tekko-no-Gyoko (Solidification of Steel)*, supplement, Solidification Comm. of ISIJ, ISIJ, Tokyo, 1977, pp. S32-S50.
42. *Metals Handbook*, 8th ed., T. Lyman, H.E. Boyer, W.J. Carnes, and M.W. Chevalier, eds., ASM, Metal Park, OH, 1973.
43. *Tekko-Binran (Handbook for Steel)*, 3rd ed., ISIJ, Maruzen, Tokyo, 1981, vol. 1, pp. 193-94.
44. W. Kurz and D.J. Fisher: *Fundamentals of Solidification*, Trans Tech Publications, Aedermannsdorf, 1989.
45. B. Sundman, B. Jansson and J.-O. Andersson: *CALPHAD*, 1985, vol. 9, pp. 153-90.
46. E. Flender: *MAGMASOFT*, Magma Gmbh, Aachen, 2000.
47. H. Jacobi and K. Wünnenberg: *Steel Res.*, 1999, vol. 70, pp. 362-67.
48. B. Weisgerber, M. Hecht, and K. Harste: *Steel Res.*, 1999, vol. 70, pp. 403-11.
49. M. Imagumbai and T. Takeda: *Iron Steel Inst. Jpn. Int.*, 1994, vol. 34, pp. 574-83.
50. D. Senk, B. Engl, O. Siemon, and G. Stebner: *Steel Res.*, 1999, vol. 70, pp. 368-72.
51. A. Suzuki, T. Suzuki, Y. Nagaoka, and Y. Iwata: *Nippon Kinzoku Gakkaishi*, 1968, vol. 32, pp. 1301-05.
52. M. El-Bealy and B.G. Thomas: *Metall. Mater. Trans. B*, 1996, vol. 27B, pp. 689-93.
53. D.J. Hurtuk and A.A. Tzavaras: *Proc. Int. Conf. on Solidification, Solidification and Casting of Metals*, University of Sheffield, Sheffield, 1977, pp. 21-28.
54. T.B. Massalski: *Binary Alloy Phase Diagrams*, ASM, Materials Park, 1986, vol. 1, p. 842.
55. V.R. Voller and S. Sundarraj: *Mater. Sci. Technol.*, 1993, vol. 9, pp 478-81.
56. A.A. Howe: *Ironmaking and Steelmaking*, 1988, vol. 15, pp. 134-42.
57. R. Flesch and W. Bleck: *Steel Res.*, 1998, vol. 69, pp. 292-99.
58. T.W. Clyne, M. Wolf, and W. Kurz: *Metall. Trans. B*, 1982, vol. 13B, pp. 259-66.
59. Y.M. Won, T. Yeo, D.J. Seol, and K.H. Oh: *Metall. Mater. Trans. B*, 2000, vol. 31B, pp. 779-94.